Materials Characterization 109 (2015) 138–151

Contents lists available at ScienceDirect

Materials Characterization

journal homepage: www.elsevier.com/locate/matchar

Gas tungsten arc welding and friction stir welding of ultrafine grained AISI 304L stainless steel: Microstructural and mechanical behavior characterization

S. Sabooni [a,*], F. Karimzadeh [a], M.H. Enayati [a], A.H.W. Ngan [b], H. Jabbari [a]

[a] Department of Materials Engineering, Isfahan University of Technology, 84156-83111 Isfahan, Iran
[b] Department of Mechanical Engineering, The University of Hong Kong, Pokfulam Road, Hong Kong, China

ARTICLE INFO

Article history:
Received 26 March 2015
Received in revised form 25 July 2015
Accepted 14 August 2015
Available online 18 August 2015

Keywords:
Friction stir welding
Ultrafine grain
Microstructure
Zener–Hollomon parameter
Sigma phase precipitate
THERMOCALC

ABSTRACT

In the present study, an ultrafine grained (UFG) AISI 304L stainless steel with the average grain size of 650 nm was successfully welded by both gas tungsten arc welding (GTAW) and friction stir welding (FSW). GTAW was applied without any filler metal. FSW was also performed at a constant rotational speed of 630 rpm and different welding speeds from 20 to 80 mm/min. Microstructural characterization was carried out by High Resolution Scanning Electron Microscopy (HRSEM) with Electron Backscattered Diffraction (EBSD) and Transmission Electron Microscopy (TEM). Nanoindentation, microhardness measurements and tensile tests were also performed to study the mechanical properties of the base metal and weldments. The results showed that the solidification mode in the GTAW welded sample is FA (ferrite–austenite) type with the microstructure consisting of an austenite matrix embedded with lath type and skeletal type ferrite. The nugget zone microstructure in the FSW welded samples consisted of equiaxed dynamically recrystallized austenite grains with some amount of elongated delta ferrite. Sigma phase precipitates were formed in the region ahead the rotating tool during the heating cycle of FSW, which were finally fragmented into nanometric particles and distributed in the weld nugget. Also there is a high possibility that the existing delta ferrite in the microstructure rapidly transforms into sigma phase particles during the short thermal cycle of FSW. These suggest that high strain and deformation during FSW can promote sigma phase formation. The final austenite grain size in the nugget zone was found to decrease with increasing Zener–Hollomon parameter, which was obtained quantitatively by measuring the peak temperature, calculating the strain rate during FSW and exact examination of hot deformation activation energy by considering the actual grain size before the occurrence of dynamic recrystallization. Mechanical properties observations showed that the welding efficiency of the FSW welded sample is around 70%, which is more than 20% higher than the GTAW welded sample.

1. Introduction

Stainless steels are undoubtedly a major and important group of structural alloys for use in different industries from low end applications such as home appliances to advanced applications such as spacecraft [1,2]. Among all types of stainless steels, austenitic stainless steels, in particular AISI 304L, are well-known due to their good corrosion resistance and great formability. Meanwhile, their relatively low hardness and yield strength is not sufficient to meet the requirements for some applications [3]. Moving towards ultrafine and nanocrystalline grain structure is one of the most effective ways to improve their mechanical properties, and as a result, ultra-fine grained (UFG) steels are currently being studied worldwide [4,5].

Weldability is one of the most important considerations for structural materials being applicable. As previously stated, UFG steels have superior properties such as improved strength and toughness in comparison with coarse grained steels. Obtaining comparable properties in the weld zone and heat affected zone (HAZ) has remained a major concern in the welding of ultrafine grained steels [6]. Grain growth in the HAZ and the existing coarse cast structure in the weld zone are the most important problems that can deteriorate the mechanical properties of the welds in UFG steels in comparison with the base metal [7]. Monte Carlo simulation has shown that the average grain size of the HAZ in a fusion welding of a 2 μm grain size steel can increase to around 120–150 μm under high heat input conditions [7]. In the recent years several methods have been applied to avoid deterioration of mechanical properties during welding of UFG steels. Usually, heat input control in the traditional welding techniques [7,8], the use of high-energy fusion welding processes such as laser welding [7], and the use of a coolant such as liquid nitrogen behind the welding zone [9], can improve the weld quality. Although these methods have been somewhat successful, deterioration of mechanical properties in the weld zone is still common. Recently, solid state welding techniques are being developed to weld advanced materials [10–12]. For

* Corresponding author.
E-mail address: s.sabooni@ma.iut.ac.ir (S. Sabooni).

http://dx.doi.org/10.1016/j.matchar.2015.08.009
1044-5803/

Table 1
Chemical composition of AISI 304L stainless steel used in this investigation.

Element	C	Cr	Ni	Mo	Mn	Si	P	S	Co	Cu	V	Fe
Wt.%	0.026	18.35	8.01	0.15	1.24	0.323	0.024	0.005	0.129	0.24	0.1	Remain

example, Miao et al. [13] studied the microstructure and mechanical properties of an MA957 nanostructured ferritic alloy welded by friction stir welding and electro-spark deposition welding. Their results showed a uniform fine scale ferrite structure with nanometer scale particles in the friction stir welded joint region that caused welding efficiency values (weld zone strength/base metal strength) of more than 90%. Chen et al. [14] also confirmed the advantages of friction stir welding of a nanostructured ODS (Oxide Dispersion Strength) material. Cho et al. [15] found that the fraction of low-angle boundaries is remarkably high in the weld nugget of 409 ferritic stainless steel which can be due to the high strain applied to the material during FSW. Ahn et al. [16] also introduced FSW as a proper welding method for 409L ferritic stainless steel due to the comparable mechanical properties and corrosion resistance of the welded zone with the base metal.

FSW has been successfully applied to aluminum as well as magnesium alloys [17,18], but only limited research has been performed to study the application of FSW in high temperature alloys such as steels, possibly due to the lack of suitable tools found for the FSW of such alloys [19]. According to the authors' knowledge, there has not been any published record on friction stir welding of ultrafine grained austenitic stainless steels and their microstructural evaluation in the weld zone. Therefore, the aim of this research is to study the microstructure and mechanical properties of FSW and gas tungsten arc welded UFG 304L stainless steels.

2. Materials and methods

UFG 304L stainless steel sheets with a thickness of 2 mm were subjected to FSW and GTAW. Table 1 shows the chemical composition of the material studied. Details of the manufacturing process of the UFG steel can be found in our previous report [20]. As shown in Fig. 1(a), the microstructure of UFG 304L stainless steel consists of a bimodal grain size distribution with an average grain size of 650 nm. The dark precipitates that can be clearly seen in the microstructure are delta ferrite. TEM micrograph of an austenite grain in the UFG sample (Fig. 1(b)) shows that the grains have large dislocation densities. GTAW was performed in fuse weld condition without any filler metal, with parameters listed in Table 2. The welding was performed under argon flow at 10 L/min.

FSW was performed using a vertical milling machine. The welding tool was made of WC with a shoulder diameter of 16 mm. A conical pin with the upper and lower diameters of 5.5 and 5 mm, respectively, and length of 1.8 mm, was used. The plates were fixed onto a steel backing plate to prevent any displacement during welding. The tilt angle of the tool was selected as 3° from the normal direction of the plate. Argon gas shield was introduced around the tool at a flow rate of 10 L/min. Welding trials were performed at a constant rotational speed of 630 RPM and different welding speeds from 20 to 80 mm/min. The schematic of the FSW geometry is shown in Fig. 2. Cross-sections ahead of the pin were selected for microstructural characterization to understand the changes of the base metal during the heating cycle of FSW. Microstructural characterization was also performed on cross-sections of the FSW welded region to understand the steady-state conditions of the welding process. The weld thermal cycles were recorded by a K-type thermocouple, which was set in a 1 mm diameter hole in the carbon steel backing plate placed exactly beneath the nugget zone center.

Microstructural characterization of the welded samples was performed using optical and scanning electron microscopy. A Field Emission Scanning Electron Microscope (FESEM, LEO 1530) equipped with electron backscattered diffraction analyzer was used to

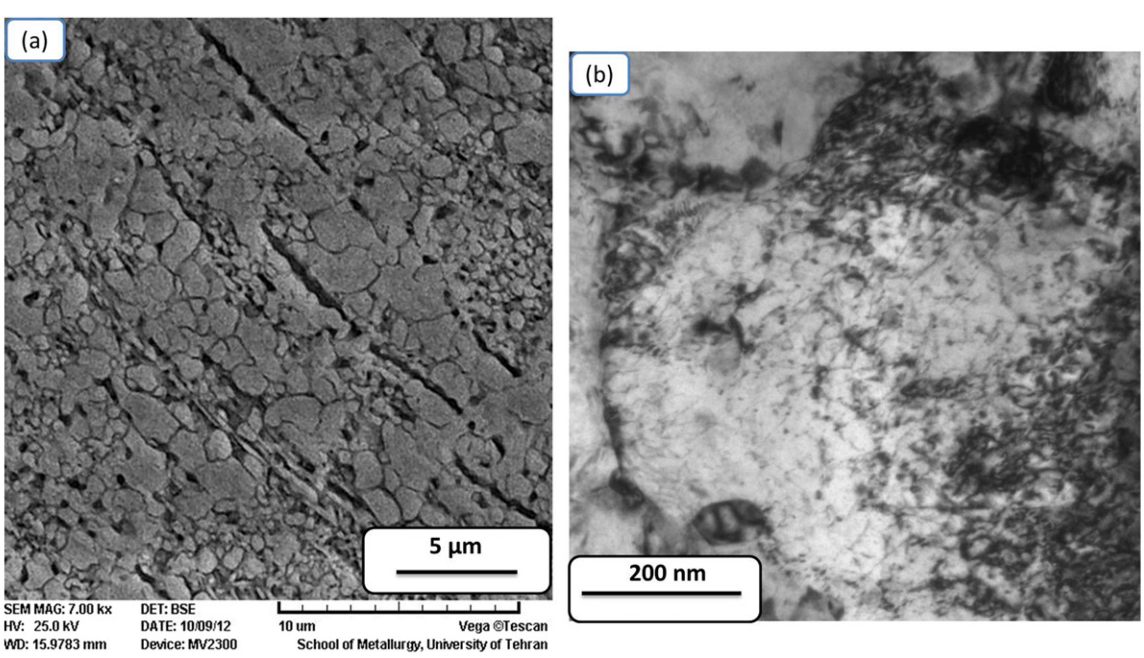

Fig. 1. SEM (a) and TEM (b) micrographs of UFG 304L stainless steel used as base metal in this investigation.

Table 2
GTAW welding conditions used in this study.

Condition	Current (A)	Voltage (V)	Argon flow (L/Min)
Fuse welding without filler metal	52	8.7	10

characterize the grain structure and to measure the average austenite grain size. Transmission Electron Microscopy of the base metal and welded samples was also performed using an FEI Tecnai G2 20 Scanning TEM. The TEM samples were produced by Focused Ion Beam (FIB) using an FEI Quanta 200 3D system from related regions of the welds. The samples were electrically etched with a solution mixture of 65% nitric acid and 35% distilled water at a voltage of 1–2 V for around 1 min to reveal the microstructures for OM and SEM. Microhardness measurements were performed using a Buehler microhardness tester with a Vickers indenter at the load of 500 gf and dwell time of 10 s. Nanoindentation tests were performed using an Agilent G200 Nanoindenter equipped with a Berkovich tip in the load control mode with maximum load of 10 mN. 25 nanoindentations were performed on selected regions of the weldments and their average was reported as the nanohardness. The thermodynamic evolution software THERMOCALC was used to calculate the equilibrium phase contents at different temperatures. The chemical composition of the studied 304L stainless steel in Table 1 was selected as input data for the thermodynamic analysis.

3. Results and discussion

3.1. Gas tungsten arc welding

Optical and SEM micrographs from the weld zone and its interface with the HAZ of GTAW welded sample are shown in Fig. 3. Low magnification micrograph (Fig. 3(a)) shows the defect free weld and its interface with HAZ. As can be seen the microstructure of the weld zone consists of ferrite and austenite, and both skeletal and lathy ferrite are visible (Fig. 3(b,c)). The results show that the solidification mode is of the FA (ferrite–austenite) type [21]. In fact the solidification starts with the initial ferrite and after that continues with austenite formation towards the end of the solidification. It should be noted that a peritectic–eutectic reaction caused austenite formation at this stage. The existence of two different δ-ferrite morphologies in the weld zone is related to the existence of different local cooling rates [21]. A skeletal ferrite morphology results when the cooling rate of the weld zone is moderate. This is a consequence of the advancement of austenite consuming the ferrite until the latter is sufficiently enriched with ferrite promoting elements (such as Cr) and depleted from austenite promoting elements (such as Ni and C) at stable conditions at lower temperatures where diffusion is limited. Meanwhile, when the cooling rate is relatively high, restricted diffusion during ferrite–austenite transformation would cause the formation of lathy instead of skeletal ferrite. In fact when the diffusion distance is reduced by a higher cooling rate, it is more possible to form lathy ferrite [21]. Epitaxial growth can be clearly seen at the interface of the weld and HAZ (Fig. 3(d,e)). In fact during welding without a filler metal, nucleation occurs by epitaxial growth without any change in crystallographic plane [21].

The microstructure of the weld can be described by studying the Cr_{eq}/Ni_{eq} ratio in relation to the solidification type. The liquidus and solidus projections of the Fe–Cr–Ni system along with the related binaries are shown in Fig. 4(a) [22]. The Fe–Cr system is isomorphous down to temperatures well below the solidification range. Also, a eutectic reaction can be observed in the Cr–Ni system at 1345 °C and 49 wt.% nickel. In the Fe–Ni system, there is a short peritectic loop containing δ-ferrite and after that the system is completely soluble. Thus, in the Fe–Cr–Ni ternary system, the liquidus projection starts with a peritectic reaction on the Fe–Ni system ($\delta + L \rightarrow \gamma$) and moves down to the eutectic reaction ($L \rightarrow \delta + \gamma$) on the Cr–Ni system. The initial solidifying phase is determined by the position of the alloy with respect to the liquidus surface. The 70 wt.% Fe isopleth of the ternary Fe–Ni–Cr system shown in Fig. 4(b) is commonly used to identify the primary solidifying phases or solidification modes for AISI 304L stainless steel [22]. The amount of Cr_{eq}/Ni_{eq} is the most effective parameter in determining the solidification mode. By increasing the ratio of Cr equivalent to Ni equivalent, the primary solidification phase changes from austenite to δ-ferrite. In the usual cooling rate range during GTAW, this change normally occurs at $Cr_{eq}/Ni_{eq} = 1.5$. It should be noted that this change in ratio is different in welding processes with more rapid cooling such as laser welding. During welding without filler metal, the weld pool consists completely of the molten AISI 304L with $Cr_{eq}/Ni_{eq} = 1.8$ and so according to Fig. 4(b), the solidification mode is FA type.

3.2. Friction stir welding

FSW was performed in order to compare the resultant microstructure and mechanical properties with the GTAW welded sample.

Fig. 5 shows a low-magnification cross sectional image of the interface of the weld nugget on the advancing side, and the thermo-mechanically affected zone (TMAZ) in the sample friction-stir welded at 80 mm/min welding speed. A banded structure is visible in the nugget zone as shown in Fig. 5(b–e) at higher magnifications. The banded region shows lower corrosion resistance in comparison with other areas of the weld as indicated by its heavily pitted surface. TEM micrograph of the corroded region in the advancing side of the weld nugget clearly shows precipitates formed both in the grain boundaries and inside the grains, while the un-corroded region does not show any precipitate formation. EDS analysis shows that these particles are Cr-rich containing 56.73% Fe, 39.6% Cr, 2.71% Ni and 0.96% Mn, in comparison with the austenite matrix containing 72.22% Fe, 18.49% Cr, 7.94% Ni and 1.35% Mn. Since no sign of carbon was detected by EDS from these particles, they cannot be chromium rich carbides. The chemical composition of these particles derived by EDS indicates that they are

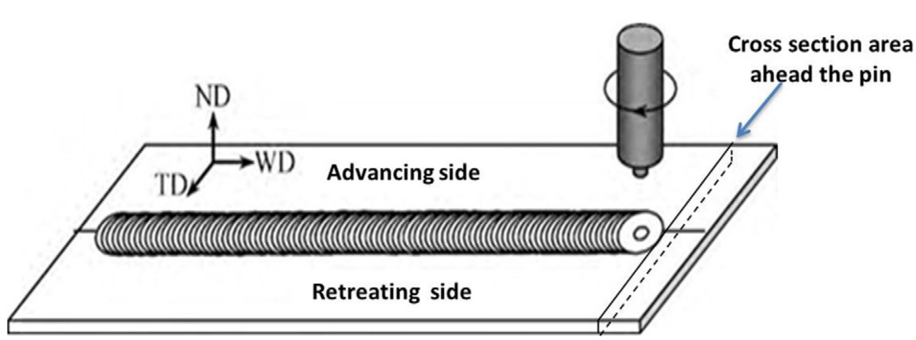

Fig. 2. Schematic illustration of the FSW welds geometry.

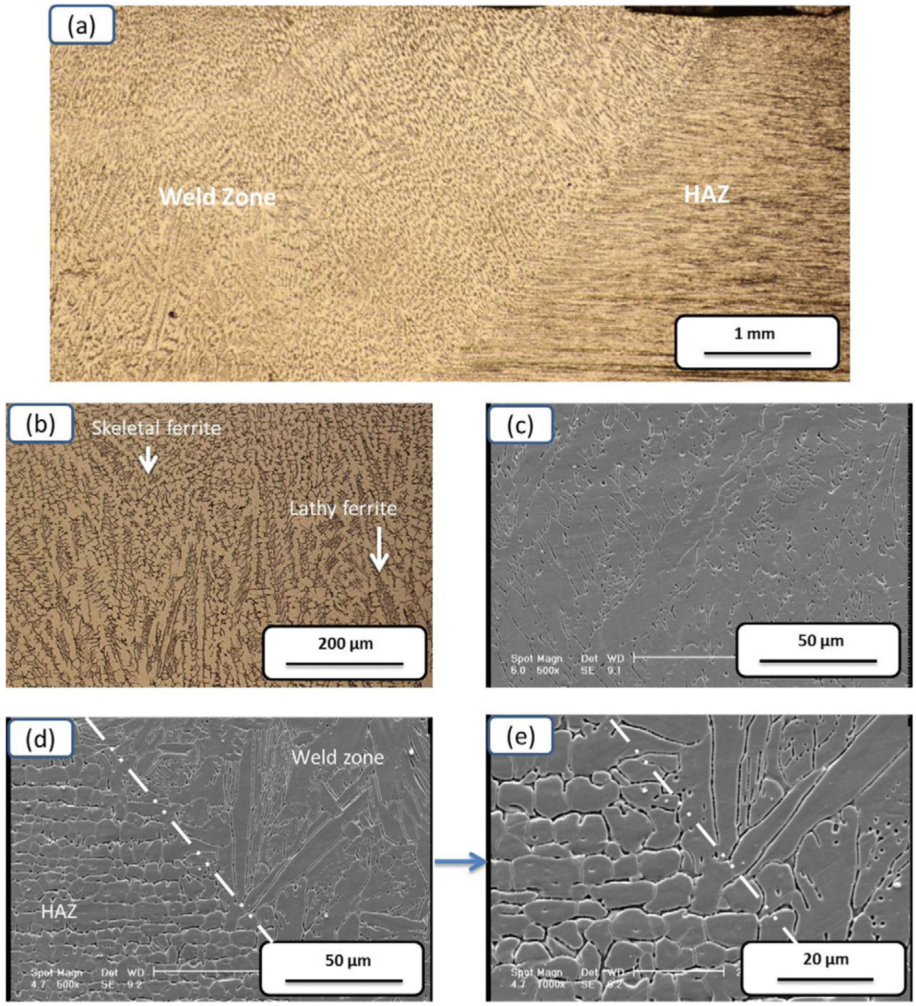

Fig. 3. Low magnification optical micrograph (a), Optical and SEM micrographs of the weld zone (b,c) and weld/HAZ interface (d,e) in the GTAW sample.

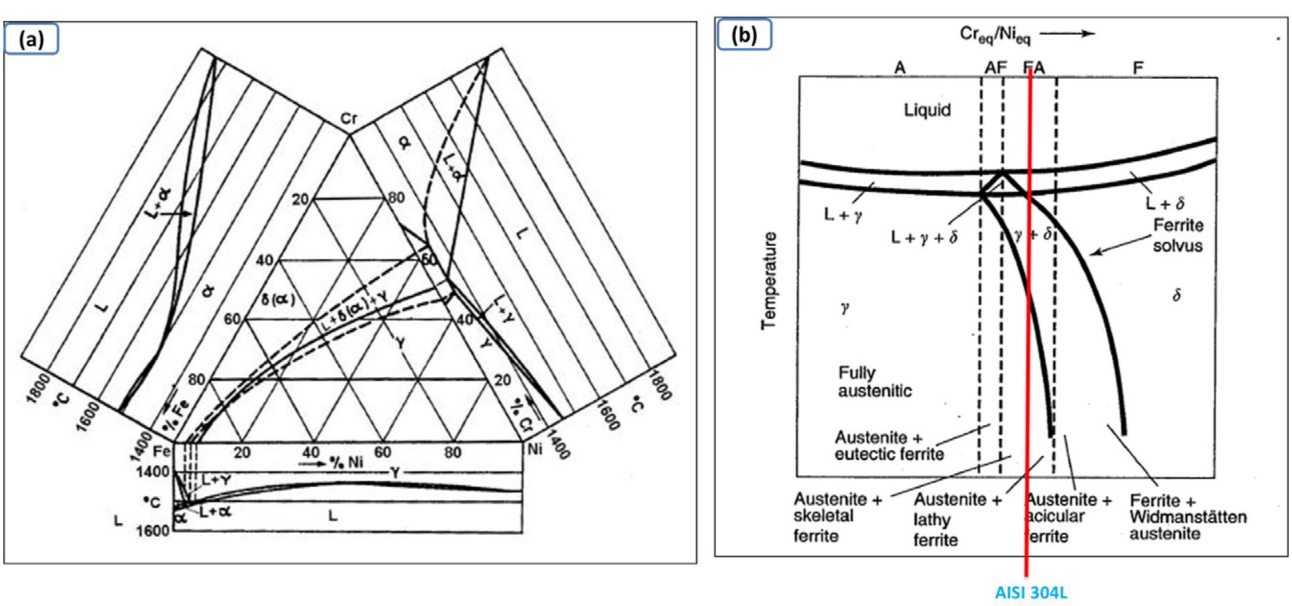

Fig. 4. (a) The liquidus and solidus projections of the Fe–Cr–Ni system along with the related binaries. (b) The 70 wt.% iron isopleth of the ternary Fe–Ni–Cr system. [22].

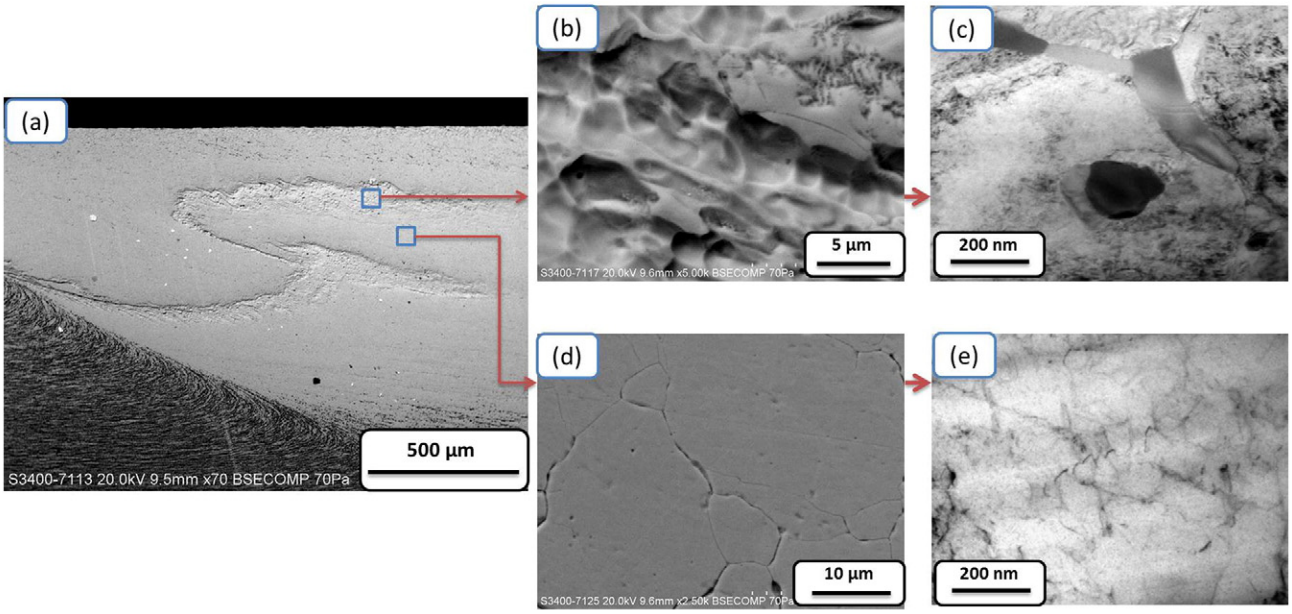

Fig. 5. (a) SEM micrograph of the banded structure in the weld nugget on the advancing side. (b and c) SEM and TEM micrographs of the corroded region inside the banded structure containing sigma phase precipitates. (d and e) SEM and TEM micrographs of the un-corroded region outside of the banded structure.

sigma phase. Image analysis of TEM micrographs shows that the austenite matrix inside the corroded region is decorated by around 12% of sigma phase particles. It should be noted that the sigma phase precipitates were only found at the low heat-input welding conditions. The formation of sigma phase during fusion welding and FSW of stainless steels has been reported earlier by several groups [23–27], although until now, the only hypothesis about the formation mechanism was proposed by Park et al. [24,25]. They suggested that the austenite grains transforms to delta ferrite at high temperatures during FSW, which can decompose again to sigma phase and austenite under high strain and recrystallization during friction stirring.

Sigma phase precipitates were found not only in the banded structure located in the advancing side of the weld nugget, but also in lower amount in the weld center. Fig. 6 shows the TEM micrographs of the sigma phase precipitates in the weld nugget center at the welding speed of 80 mm/min. It can be seen that the sigma phase is formed both in the austenite and delta ferrite matrix. The width of sigma phase particles is less than 200 nm. The reasons for sigma phase formation will be described in greater details below.

Nanoindentation experiments were carried out to study the effect of sigma phase formation on the hardness of the banded area in comparison with other regions of the weld nugget. Fig. 7 shows typical examples of load–displacement curves out of 25 repeated nanoindentation tests on the banded area containing sigma phase precipitates and the un-corroded region comprising austenite grains. The Oliver–Pharr method [28] was used to calculate the hardness from the load–displacement curves. The nano-hardness of the banded area and the un-corroded regions were calculated as 5.2 GPa and 4.4 GPa, respectively, which show that sigma phase precipitation effectively increases the hardness of the banded area. It was also found that the sigma phase precipitates which are effectively distributed as a continuous structure in the grain boundaries can considerably reduce the amount grain growth of the banded area during subsequent annealing of the welded samples. Fig. 8 shows the SEM micrographs of the corroded and un-corroded regions in Fig. 5(a) after subsequent annealing at 1000 °C for 60 min. Considerable grain growth has occurred in the un-corroded region where the average grain size increased from 13 μm before annealing to around 40 μm after annealing. Meanwhile, sigma phase precipitates retard growth of the austenite grains in the corroded region. Therefore, despite the fact that sigma phase is known to be detrimental to the corrosion resistance of welded samples of austenitic stainless steels [24,25,29], it has the advantage of increasing the hardness and thermal stability of the material.

The THERMOCALC software was used to study the equilibrium condition of sigma phase precipitation in the investigated alloy. Although the result of equilibrium condition may be a little different from the actual processing condition, it can still be useful to understand the precipitation temperature range of sigma phase during welding. Fig. 9 shows the equilibrium precipitation data for the sigma phase calculated by the THERMOCALC software. As can be seen, the temperature range of 600 °C–700 °C is the most possible range for sigma phase precipitation which matches well with the thermal profile of the FSW welded sample with the welding speed of 80 mm/min. The results of THERMOCALC analysis also show that no sigma phase should form at temperatures higher than 770 °C, which means that sigma phase precipitates should dissolve in the matrix at such high temperatures. This explains the absence of sigma phase in the weld nuggets of samples welded using high heat input conditions.

Microstructural evolution of the regions ahead the welding tool was studied to understand the on-going events there before the occurrence of dynamic recrystallization, and to find out the reasons for sigma phase formation in the weld nugget. From EBSD, the microstructure just ahead of the welding tool was identified as austenite grains with a small amount of delta ferrites which are present from the base metal (Fig. 10(a)). It was found that the grain growth has occurred in comparison with the UFG base metal during the heating cycle of FSW (Fig. 10(b)). EBSD results also showed that the actual grain size before the occurrence of dynamic recrystallization during the heating cycle of FSW varies between 3 μm at the welding speed of 20 mm/min to 1.5 μm at the welding speed of 80 mm/min.

TEM samples were cut from the regions ahead of the rotating tool for samples welded at the welding speed of 20 mm/min and 80 mm/min, in order to detail examination the phase transformation and microstructural evolution during the heating cycle of FSW. Fig. 11 shows the TEM micrograph of typical precipitates present in the region ahead the welding tool at the welding speed of 80 mm/min. Line scan shows that these precipitates are Cr rich with lower amounts of Fe and Ni in comparison with the matrix. EDS analysis shows that these particles are sigma phase containing 39% Cr, 56.48% Fe, 2.52% Ni, 1.24% Mn and 0.76% Si, which exhibits the same chemical composition as the particles found in the banded structure (Fig. 5(c)). It should be noted that no sign

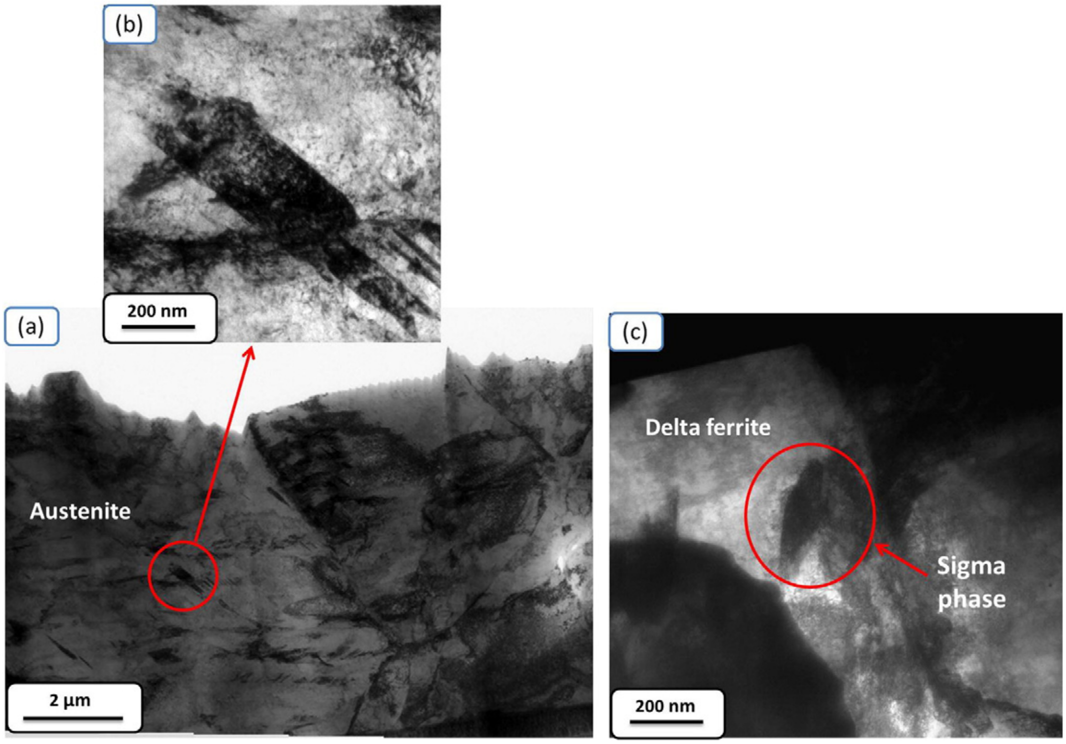

Fig. 6. TEM micrographs showing sigma phase formation in the austenite (a and b) and delta ferrite grains (c) in the weld center of sample friction stir welded at the welding speed of 80 mm/min.

of sigma phase was detected in the UFG base metal and therefore it can be considered that the particles are formed during the heating cycle of the FSW with the movement of the rotating tool. The size of sigma phase particles in this stage was found to be around several hundred nanometers which is different from the size of sigma phase particles found in the weld nugget after FSW (around 100 nm or less).

There is the possibility that the sigma phase precipitates after FSW are related to the sigma phase ahead the rotating tool formed during the thermal cycle of FSW — stirring of the weld nugget may fragment the existing large sigma phase particles into nanometric precipitates in the weld nugget zone. However, this mechanism alone cannot justify the concentration of sigma phase particles in the advancing side of the weld nugget. Therefore, in addition to this mechanism, some other mechanism for the sigma phase formation should also occur. Since, sigma phase is a Cr rich precipitate rather than austenite (FCC) and delta-ferrite (BCC), its formation is a diffusion controlled process that needs Cr atoms diffusion within grains or along grain boundaries [29]. It is reported that the formation of sigma phase in austenitic stainless steels is not readily observable when the Cr content is less than 20%. However, its formation can be accelerated by 100 times, with increasing

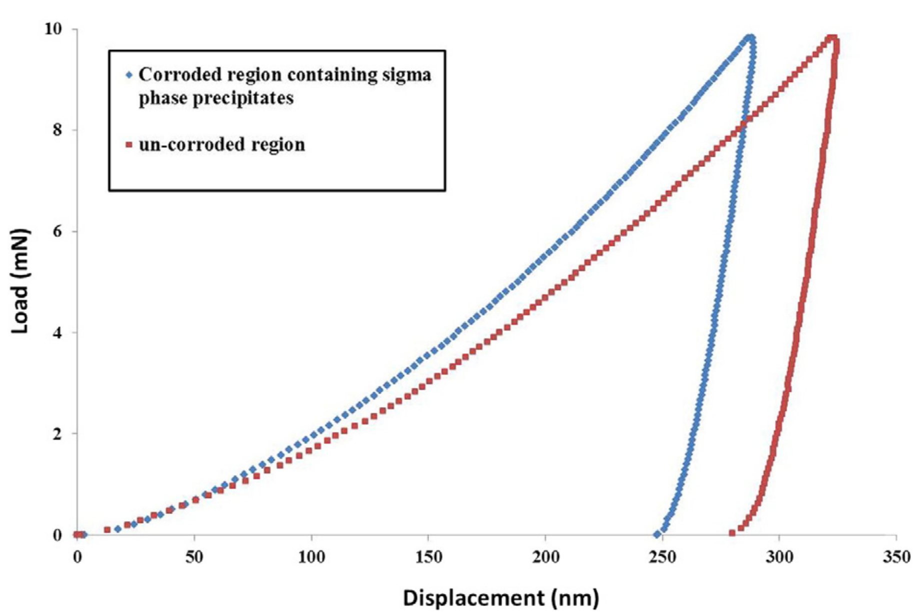

Fig. 7. Load–displacement nanoindentation curve of the corroded and un-corroded regions of the banded structure.

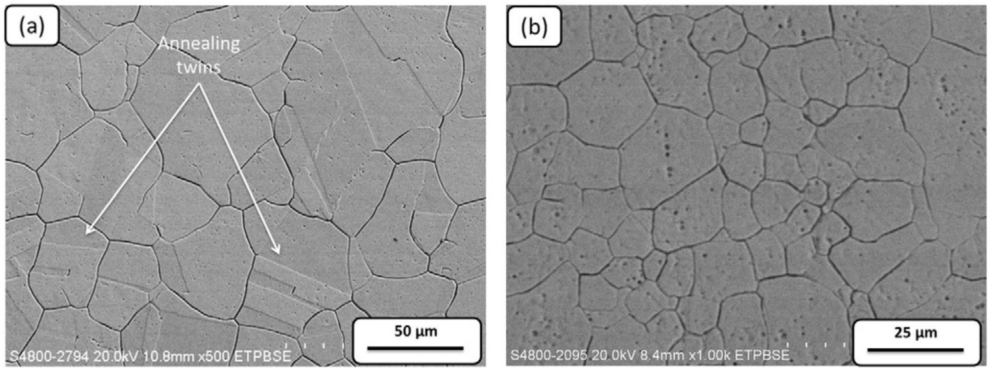

Fig. 8. SEM micrographs of the corroded and un-corroded regions of Fig. 5(a) after subsequent annealing at 1000 °C for 60 min.

the Cr content to around 25%–30 wt.%, since a higher Cr content decreases the necessity of atomic diffusion to form sigma phase [29]. In other words, although the direct formation of sigma phase from austenite is thermodynamically possible, it would normally take several tens of hours that are not available in the FSW condition. For example, the start of sigma phase precipitation in single phase 321 stabilized austenitic stainless steel was detected as 72 h at the temperature of 973 K [30]. It can be concluded that the existing of delta ferrite in the microstructure can play an important role in the formation of sigma phase. However the decomposition of delta ferrite to sigma phase during ordinary aging at 700 °C takes at least 0.5 h which is much longer than the holding time in the FSW [31]. It was also reported [32,33] that high strain and occurrence of recrystallization can considerably accelerate sigma phase formation. For example, Ameyama et al. [32] have reported that ferrite grains rapidly transforms to sigma phase in a micro duplex (ferrite and austenite) structure produced by high strain powder milling during sintering. Vitek and David [33] have also confirmed the positive effect of recrystallization on the sigma phase formation during the aging of 308 austenitic stainless steels. Since FSW introduces high strain into the material at a high temperature and it is accompanied with recrystallization, there is a high possibility that the existing delta ferrite in the microstructure rapidly transforms into sigma phase particles during the short thermal cycle of FSW.

Some amount of recovery also took place in the region ahead the rotating tool at the welding speed of 20 mm/min, which was not observed at the welding speed of 80 mm/min. The formation of dislocation cells which are visible in the TEM micrographs of Fig. 12(a and b) can confirm that existence of dynamic recovery beside grain growth at the welding speed of 20 mm/min. In other words, higher heat input at the slower

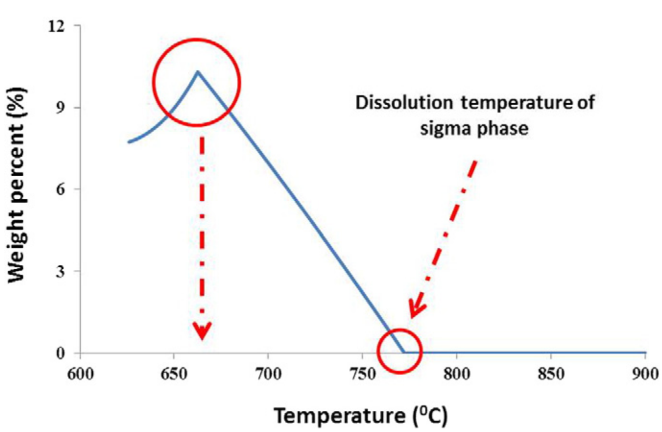

Fig. 9. Equilibrium sigma phase precipitation data in the temperature range of 600–900 °C obtained by THERMOCALC analysis.

welding speed of 20 mm/min promotes recovery besides grain growth, while only grain growth alone without considerable recovery occurred at the welding speed of 80 mm/min before occurrence of dynamic recrystallization.

Fig. 13 shows the temperature profiles recorded at the constant rotational speed of 630 RPM and different welding speeds during FSW. It can be seen that the peak temperature is 960, 865, 770 and 720 °C for the welding speeds of 20, 32, 50 and 80 mm/min, respectively. As can be seen the peak temperature decreases with increasing welding speed. Similar results were reported in the welding of duplex stainless steels [34-35]. It can be concluded that the welding speed has a significant effect on the thermal profile and finally on the microstructure and mechanical properties of the welds. The microstructure of the weld nugget depends on the peak temperature and cooling rate during FSW. Meanwhile, these factors are controlled by process parameters such as the rotational and welding speeds that can finally determine the total heat input during FSW. Frigaard et al. [36] proposed the following equation for the net heat input (Q) during FSW:

$$Q = \left(\frac{4}{3}\right)\pi^2 \mu P \omega R^3 \tag{1}$$

where μ is the friction coefficient, P is the applied pressure (Pa), R is the tool shoulder radius (m), and ω is rotational speed of the tool (Rev/s). In this study we could not measure the real friction coefficient and vertical pressure quantitatively. Furthermore, it is reported that the applied pressure is almost constant when the plunge depth during FSW is constant, and also, the friction coefficient during FSW is always constant. The heat input per unit length of the weld can be obtained by dividing the total heat input, Q, to the welding speed, υ, namely (Q/υ), and since μ, P and R are constant, (Q/υ) is proportional to (ω/υ). So, it is clear that the increasing of the welding speed causes decreasing of the heat input per unit length. It was also demonstrated [34-35] that the peak temperature T_P (changes with υ and ω according to:

$$\left(\frac{T_P}{T_m}\right) = K\left(\frac{(\omega^2)}{\left(\upsilon \times 10^4\right)}\right)^{\alpha} \tag{2}$$

where T_m is the melting point of the alloy being welded (, and K and α are constants. From Eq. 2 and the results of the thermal profile in Fig. 13, a simplified relation between T_p and υ is as follows:

$$T_p = 1800\left(\frac{1}{v}\right)^{0.213}. \tag{3}$$

Results of EBSD analysis of the samples welded at 20 mm/min and 80 mm/min are shown in Fig. 14. It should be noted that the EBSD analysis was performed at the weld center on the ND-TD plane (transverse

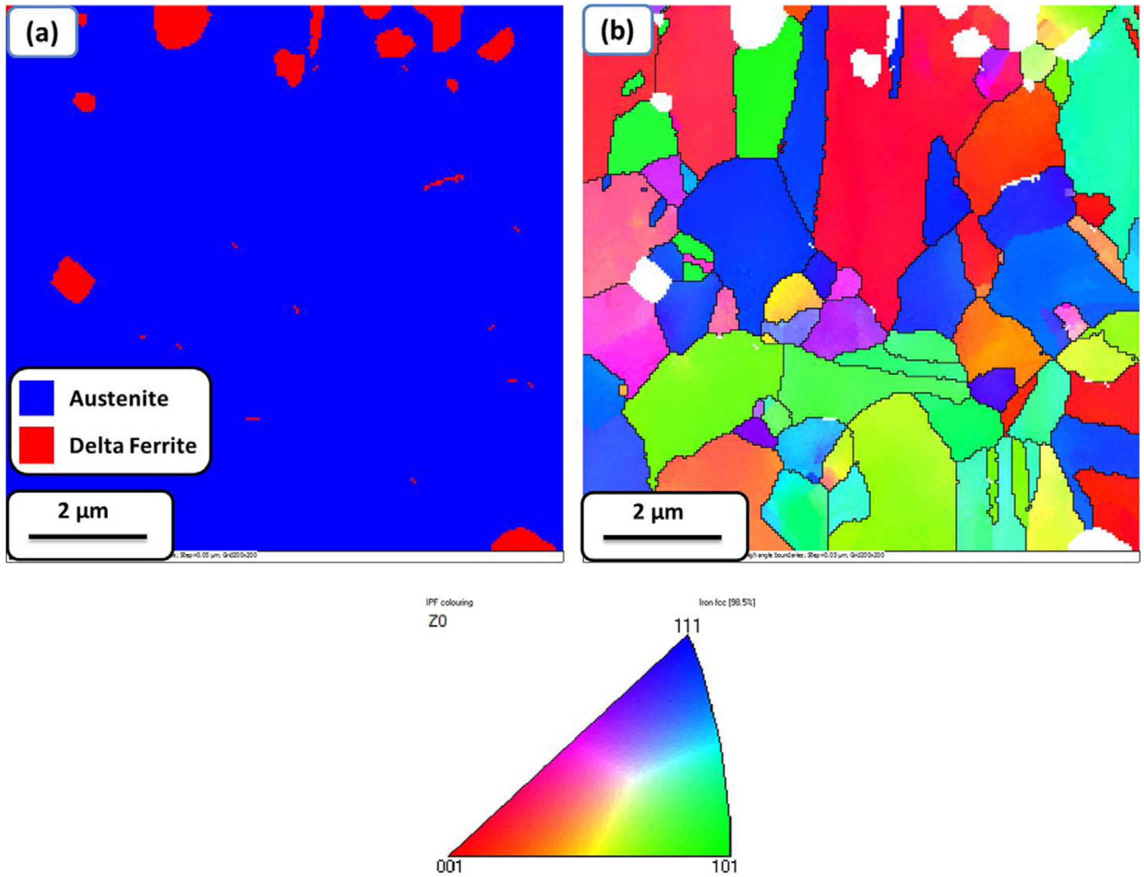

Fig. 10. (a) Phase map and (b) Inverse Pole Figure (IPF) map of the region just in the front of the tool pin before the occurrence of dynamic recrystallization at the welding speed of 20 mm/min.

cross section). The microstructure of both samples in the weld center consists mostly of equiaxed austenite grains with a small amount of delta ferrite. EBSD analysis shows that the amount of delta ferrite increases from 2% at the welding speed of 20 mm/min to 7% at the welding speed of 80 mm/min. It seems, therefore, that at the higher temperature at the slower welding speed of 20 mm/min, most of delta

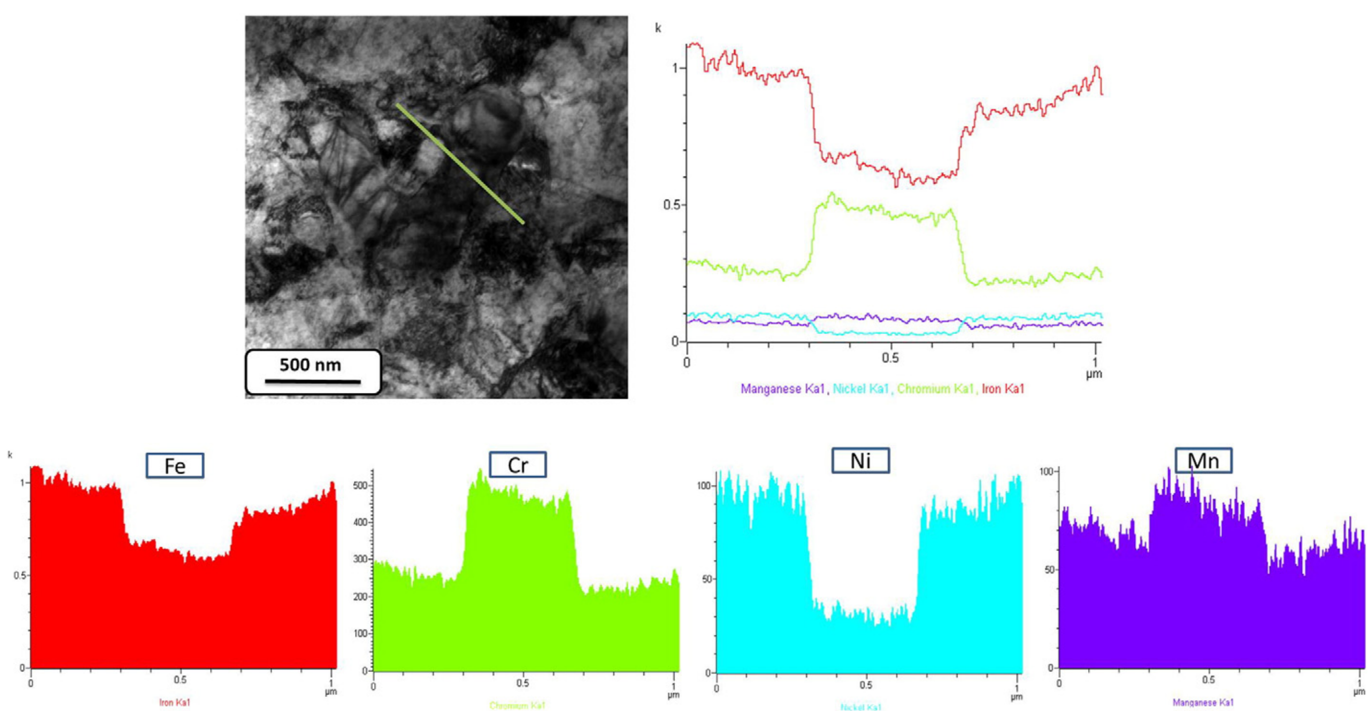

Fig. 11. Typical TEM micrograph of sigma phase precipitates in the regions ahead the welding tool at the welding speed of 80 mm/min along with line scan profiles of major elements.

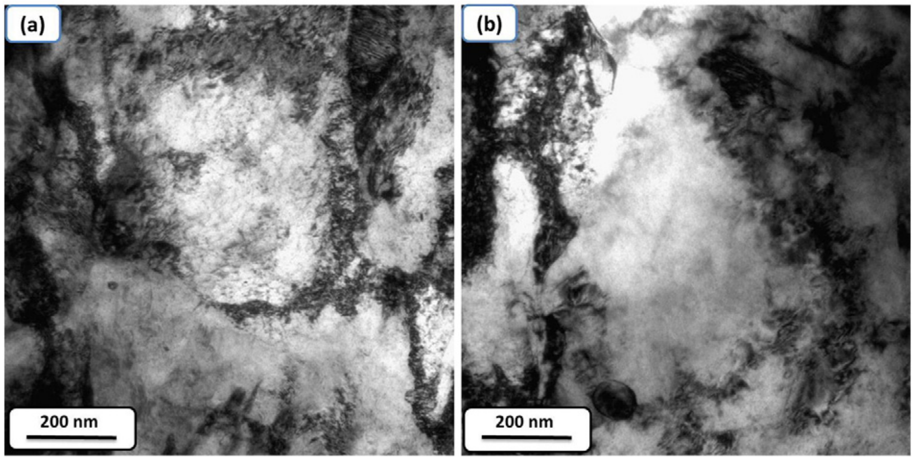

Fig. 12. TEM micrographs of the region just ahead the welding tool at the welding speed of 20 mm/min.

ferrites are dissolved in the austenite grains. For the sample welded at 20 mm/min, the average austenite grain size was found to be 21 μm with a standard deviation of around 9.5 μm. The fraction of grains having size larger than 35 μm is just 9%. The largest and smallest grain size observed from the EBSD micrograph is 42 and 7 μm, respectively. Meanwhile the average grain size for the sample welded at 80 mm/min was found to be 11 μm with a standard deviation of 3.7 μm. In this case, the largest and smallest grain size was found as 21 and 5 μm, respectively. The presence of fine equiaxed austenite grains is related to the occurrence of dynamic recrystallization during FSW [37]. Also, it can be seen that the grain size after welding at 20 mm/min is higher than that at 80 mm/min which should be due to the excess heat input at the slower welding speed.

The FSW process is in fact a kind of thermomechanical process because during FSW, the material undergoes intense plastic deformation at elevated temperatures and this can be accompanied by dynamic recrystallization to finally produce a fine microstructure. Under the severe plastic deformation during FSW, the austenite grain size depends on the strain rate and the temperature. The combined effect of these two parameters can be represented by the Zener–Hollomon parameter as follows [38]:

$$Z = \dot{\varepsilon}\ \exp\left(\frac{Q_A}{RT}\right) \tag{4}$$

where $\dot{\varepsilon}$ is the strain rate, T is temperature, R is gas constant and Q_A is the hot deformation activation energy. According to the flow pattern modeled by Reynolds [39], the approximate strain experienced by the material during FSW can be expressed as:

$$\varepsilon = \mathrm{Ln}\left(\frac{L}{\mathrm{APR}}\right) + \left|\ \ln\left(\frac{\mathrm{APR}}{L}\right)\right| \tag{5}$$

where APR is the tool advancement per revolution, and L can be calculated as

$$L = 2r\ \ \cos^{-1}\left[\frac{r-a}{r}\right] \tag{6}$$

where r is the pin diameter and a is the distance from the advancing to retreating side of the tool where material flows into this region. Considering the value of $r = 5$ mm and $a = r$, $L = 15.7$ was used for all samples. Finally the strain rate can be calculated as

$$\dot{\varepsilon} = \frac{\varepsilon}{t} \tag{7}$$

where t is deformation time that can be expressed as $t = \frac{r}{v}$.

The value of the activation energy Q_A for hot deformation for coarse grained AISI 304 is about 400 kJ/mol [40]. Grain size has a considerable effect on the value of Q_A and so the mentioned value should not be valid for UFG 304 stainless steel. For example, the values of Q_A for 304

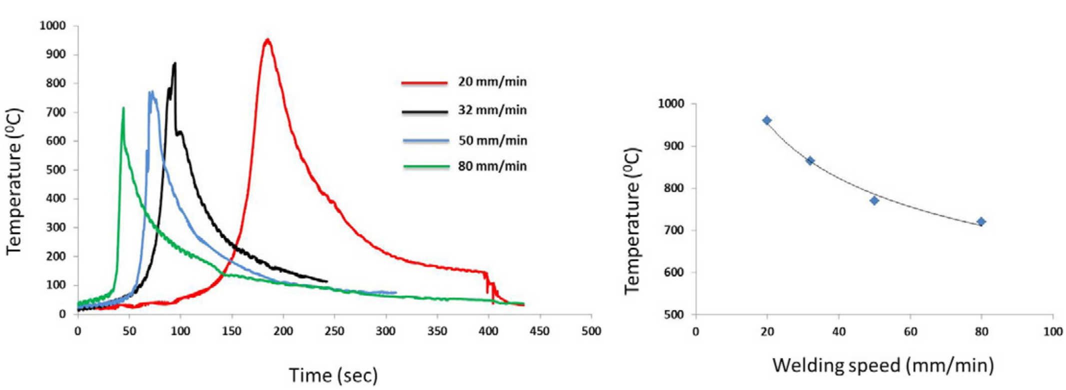

Fig. 13. (a) Measured thermal profiles during different FSW trials, and (b) the change of peak temperature with welding speed at the constant rotational speed of 630 rpm.

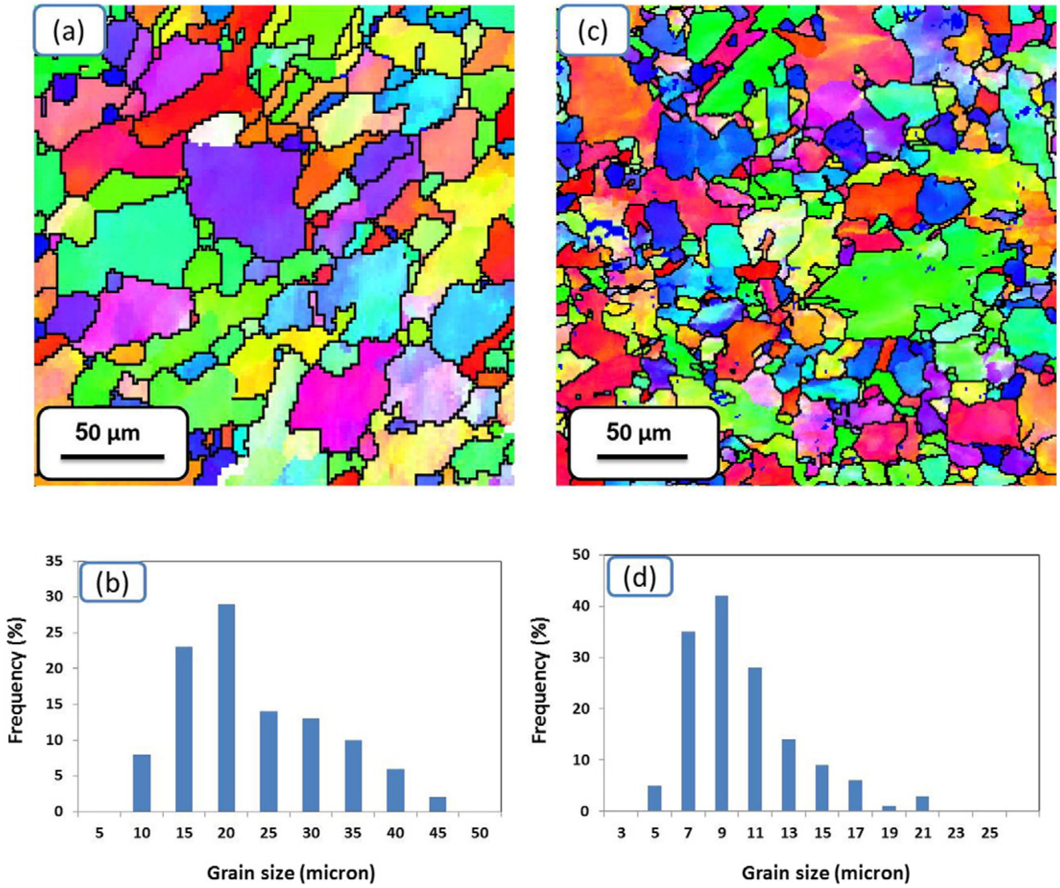

Fig. 14. EBSD map and grain size distribution of the weld center for the samples FSW at 20 mm/min (a–b) and 80 mm/min (c–d).

stainless steel with grain size of 8 and 35 μm are about 354 and 457 kJ/mol, respectively [41]. Parsa et al. [41] suggested the following equation for the relationship between the Q_A of AISI 304 and the grain size (GS):

$$Q_A = 287.5(GS)^{0.1}. \tag{8}$$

Because of the excess stored energy in the grain boundaries of UFG 304L stainless steel, this material tends to exhibit grain growth during the heating cycle of FSW [42]. As stated previously, our observation shows that the grain size in the front of the rotating pin and before the occurrence of dynamic recrystallization is not the same as the base metal. Therefore, in order to more accurately calculate the activation energy, the actual grain size obtained by EBSD was used in Eq. (8). The calculated parameters using Eqs. (4)–(8) are summarized in Table 3. Also, the austenite grain size in the stirred zone after FSW is finally related to the Zener–Hollomon parameter in Fig. 15. The Zener–Hollomon parameter that includes the effects of both the deformation temperature and strain rate controls the stored energy in the hot deformation process which is an important factor influencing the recovery and recrystallization during FSW and hence the final grain size [38]. As can be seen in Fig. 15, the austenite grain size after FSW decreases with increasing Zener–Hollomon parameter. A similar trend was also observed in the FSW of M 190 ultrahigh strength steels [38]. The variation of the austenite grain size after FSW in Fig. 15 is well represented by the linear relationship of

$$\frac{1}{d} = 0.0062 \text{ Ln } (Z) - 0.1456. \tag{9}$$

3.3. Mechanical property evolution

Fig. 16 compares the microhardness values of the weld center under different welding conditions. As can be seen the microhardness value of the base metal is 330 HV and all welds show lower hardness than the UFG base metal. Increasing the welding speed in FSW causes a considerable increase in the microhardness and this is related to the lower grain size obtained by a reduction of the heat input. The microhardness of the weld zone in the sample welded at 80 mm/min is 285 HV which is much higher than that for the samples welded by GTAW. A considerable decrease in the weld zone microhardness of UFG plain carbon steel and UFG-IF steel was observed respectively by Ueji et al. [43] and Sun et al. [44] after FSW. These reductions can be related to the grain growth caused by the welding heat, and as stated previously, decreasing the heat generated during welding can considerably affect the microstructure and resultant mechanical properties.

The microhardness evolution was also investigated along the transverse cross section of the weldments (ND-TD plane) which is shown in the Fig. 17. As can be understood, the lowest hardness of the GTAW sample occurs inside the welded zone where a coarse grain cast structure is produced through a solidification process. The hardness of the GTAW sample increases gradually on moving away from weld zone towards the HAZ and the base metal. As shown in Fig. 3(d and e), the microstructure of the HAZ in the GTAW sample is characterized by equiaxed grains which formed from grain growth of the initial ultra fine grains of the base metal. The amount of grain growth is lower in the regions far from the welded zone since these regions experienced lower temperatures. This is why the hardness of the GTAW sample increases with increasing distance from the weld center. Interesting, the microhardness profile of the FSW sample is not the same as that of

Table 3
Summary of calculated peak temperature, strain, strain rate, Zener–Hollomon parameter and austenite grain size in different FSW conditions.

Welding speed	Peak temperature at weld nugget (°C)	Strain (%)	Strain rate (s^{-1})	Z (s^{-1})	Austenite grain size after FSW in the weld center (μm)
20	960	12.41	0.827	2.98×10^{13}	21
32	865	11.46	1.223	3.5×10^{14}	15
50	770	10.57	1.760	4.7×10^{15}	13
80	720	9.63	2.57	1.55×10^{16}	11

the GTAW sample, with the lowest hardness occurring in the HAZ region. The average hardness of the weld nugget in the FSW sample at the welding speed of 80 mm/min is around 285 HV, which is nearly constant within the weld nugget. Meanwhile, the lowest hardness which is 260 HV occurs in the HAZ region adjacent to the TMAZ. EBSD was performed on the TMAZ and HAZ regions to characterize the grain structure there, but it did not show any considerable difference. TEM samples were extracted from related regions of TMAZ and HAZ in order to study the substructures there. Fig. 18(a) and (b) show the TEM micrographs of the TMAZ and HAZ, respectively. Fig. 18(c and d) show EDS and Selected Area Diffraction (SAD) results of the the precipitates present in Fig. 18(a). These observations show that the precipitates present are Cr rich, with 29 wt.% Cr compared to ~18 wt.% in the surrounding matrix, and exhibit a BCC structure which was finally identified as delta ferrite. Nano-twins can clearly be observed in the TMAZ region which are absent in the HAZ region. The temperature and strain in the TMAZ are not as high as in the weld nugget to allow dynamic recrystallization, but it seems that the stress in the TMAZ is sufficient to cause the formation of mechanical twins. Therefore, it seems that the higher hardness of the TMAZ in comparison with the adjacent HAZ is due to the mechanical twins formed during the deformation in the TMAZ.

Fig. 19 shows the engineering stress–strain curves of the UFG base metal, GTAW sample and FSW sample at the welding speed of 80 mm/min. It should be noted that the tensile specimens were cut in the transverse direction of the welded samples. The UFG base metal shows a yield strength of 720 MPa, ultimate tensile strength (UTS) of 920 MPa and tensile elongation of around 47%. Both the GTAW and FSW samples show lower yield strength and UTS than the UFG base metal. The existence of a cast coarse grained structure in the GTAW weld zone causes considerable drop in the mechanical properties of the weld so that the yield strength drops to 340 MPa which is just 47% of that of the base metal. Meanwhile, the existence of fine dynamically recrystallized grains in the weld nugget of the FSW sample along with the distribution of nanometric sigma phase precipitates lead to an increased yield strength to 500 MPa, which means a welding efficiency of 70%. Final rupture occurred at the weld zone in the GTAW welded sample while occurred in HAZ in the FSW welded samples. It is consistent with the results of microhardness measurements where the minimum hardness located in the weld zone in GTAW while located in HAZ during FSW. The results of microhardness profile and tensile tests confirm that FSW is an alternative and potentially better welding procedure for the welding of UFG steels rather than conventional fusion welding methods.

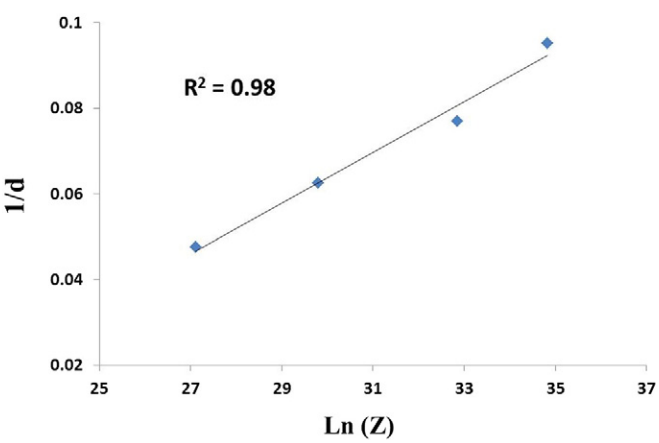

Fig. 15. Variation of austenite grain size after FSW versus Zener–Hollomon parameter.

4. Conclusions

An ultrafine grained AISI 304L was successfully welded by both gas tungsten arc welding and friction stir welding techniques. The results showed that significant differences were present between the microstructures of the FSW and GTAW welded samples. The microstructure of GTAW welded sample shows a cast microstructure consisting of austenite and ferrite, which both lathy and skeletal ferrite present. Friction-stir welded samples exhibited a microstructure consisting of fine equiaxed austenite grains along with some elongated δ-ferrite. TEM observations showed that nanometric sigma phase precipitates were formed in the weld nugget, which were mostly distributed as a continuous structure at grain boundaries in the advancing side of the weld nugget forming a banded structure in the transverse cross section. It seems that the sigma phase precipitates were initially formed at the regions ahead the rotating tool during the heating cycle of FSW, and were finally fragmented into nanometric particles in different regions of the

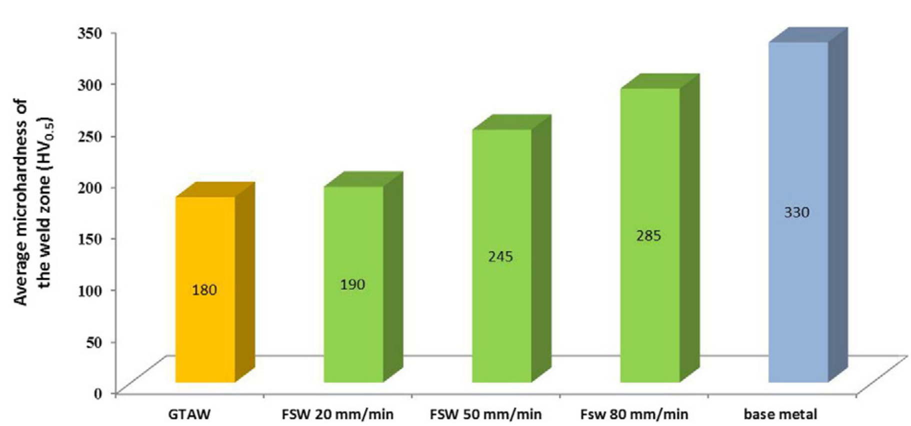

Fig. 16. Average microhardness values of the base metal and the weld zone produced under different welding conditions.

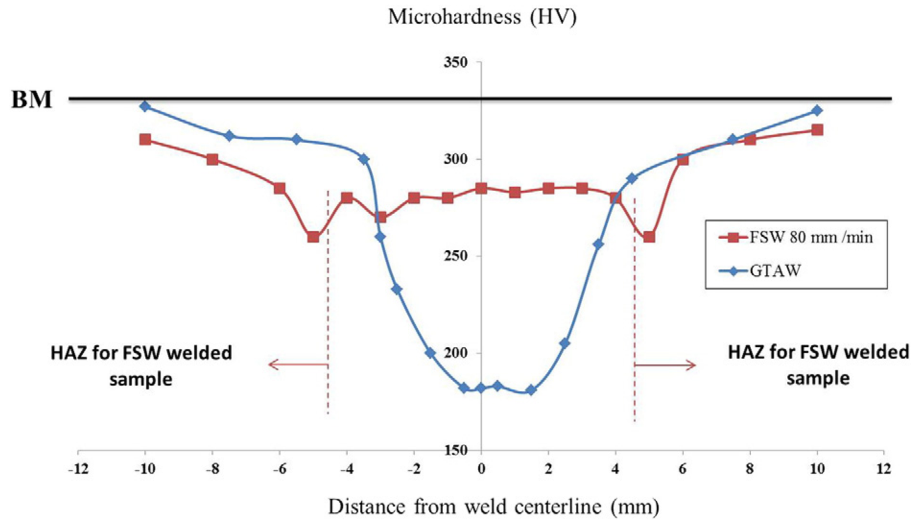

Fig. 17. Microhardness distribution of the GTAW and FSW samples along transverse cross section (ND-TD plane) of the weldment.

weld nugget. Also there is a high possibility that the existing delta ferrite in the microstructure rapidly transforms into sigma phase particles during the short thermal cycle of FSW. It was found that the existence of strain and recrystallization can promote sigma phase formation. THERMOCALC analysis showed that the temperature range of 600–700 °C is the most possible range for sigma phase precipitation which agrees with experimental results. The final austenite grain size in the nugget zone of the friction-stir welded samples was found to be a function of the Zenner–Hollomon parameter obtained quantitatively by measuring the peak temperature and calculating of the strain rate

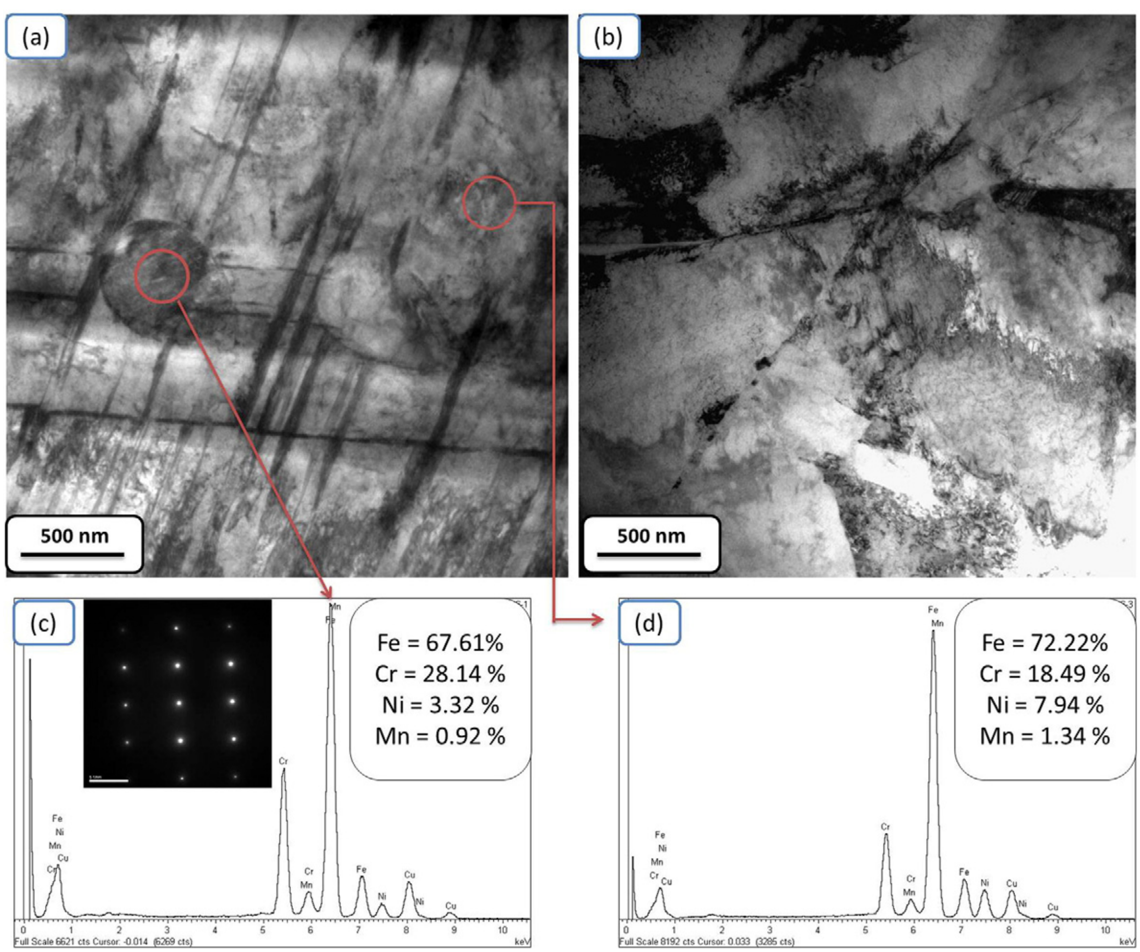

Fig. 18. TEM micrographs of the TMAZ (a) and HAZ (b) in the sample welded at the welding speed of 80 mm/min showing the existence of mechanical twins in the TMAZ, along with EDS and SADP of particles (c) and matrix (d) of TMAZ.

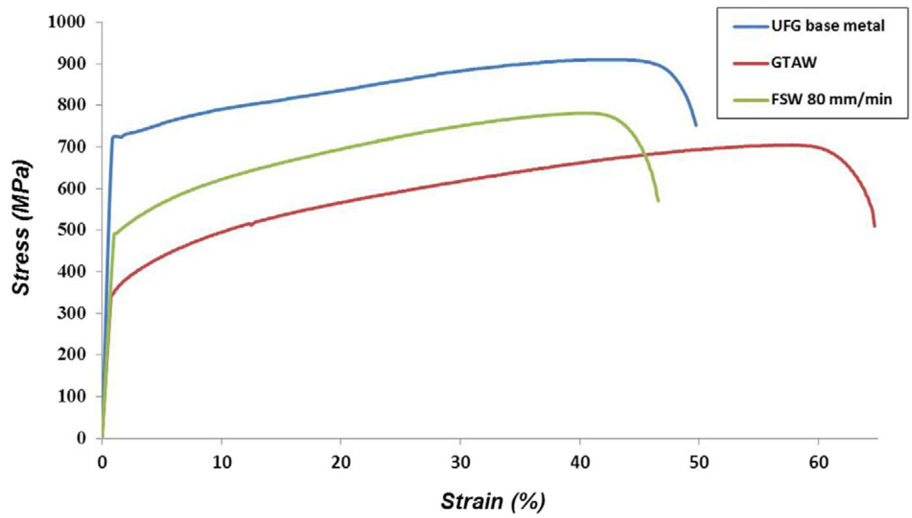

Fig. 19. Engineering stress–strain curves of the UFG base metal and welded samples.

during the welding process. A considerable reduction in grain size was observed with increasing Zener–Hollomon parameter caused by an increase in welding speed. Microhardness evolution along the transverse cross section of the weldments showed that the minimum hardness of the GTAW sample occurred at the weld center, while this occurred at the HAZ in the FSW samples. Mechanical property evolution confirmed that FSW is an alternative, or even better, welding technique for the welding of ultrafine grained steels than conventional fusion welding processes.

References

[1] R.L. Plaut, C. Herrera, D.M. Escrib, P.R. Rios, A.F. Padilha, A short review on wrought austenitic stainless steels at high temperatures: processing, microstructure, properties and performance, Mater. Res. 10 (4) (2007) 453–460.
[2] J.R. Davis, ASM Specialty Handbook: stainless steel, metals Park, OH, 1994.
[3] L.P. Karjalainen, T. Taulavuori, M. Sellman, A. Kyröläinen, Some strengthening methods for austenitic stainless steels, Steel Res. Int. 79 (6) (2008) 404–412.
[4] S. Sabooni, F. Karimzadeh, M.H. Enayati, A.H.W. Ngan, The role of martensitic transformation on bimodal grain structure in ultrafine grained AISI 304L stainless steel, Mater. Sci. Eng. A 636 (2015) 221–230.
[5] M. Shirdel, H. Mirzadeh, M.H. Parsa, Nano/ultrafine grain austenitic stainless steel through the formation and reversion of deformation-induced martensite: mechanisms, microstructures, mechanical properties, and TRIP effect, Mater. Charact. 103 (2015) 150–161.
[6] S. Sabooni, F. Karimzadeh, M.H. Enayati, A.H.W. Ngan, Friction stir welding of ultrafine grained austenitic 304L stainless steel produced by martensitic thermomechanical processing, Mater. Des. 76 (2015) 130–140.
[7] Y. Weng (Ed.), Ultrafine grained steels, Springer, Beijing, 2009.
[8] Y. Peng, Z. Tian, C. He, X. Zhang, H. Xiao, Effect of welding thermal cycle on the microstructure and mechanical properties of ultra-fine grained carbon steel, Mater. Sci. Forum 426–432 (2003) 1457–1462.
[9] H. Hamatani, Y. Miyazaki, T. Otani, S. Ohkita, Environmental conscious ultra-fine-grained steel consortium of JRCM (The Japan Research and Development Center of Metals), minimization of heat-affected zone size in welded ultra-fine grained steel under cooling by liquid nitrogen during laser welding, Mater. Sci. Eng. A 426 (2006) 21–30.
[10] R. Nandan, T. DebRoy, H.K.D.H. Bhadeshia, Recent advances in friction-stir welding — process, weldment structure and properties, Prog. Mater. Sci. 53 (2005) 980–1023.
[11] M.C. Chaturvedi, Welding and joining of aerospace materials, Woodhead Publishing, 2012.
[12] Dan Wang, Jun Shen, Lin-zhi Wang, Effects of the types of overlap on the mechanical properties of FSSW welded AZ series magnesium alloy joints, Int. J. Miner. Metall. Mater. 19 (3) (2012) 231–235.
[13] P. Miao, G.R. Odette, J. Gould, J. Bernath, R. Miller, M. Alinger, C. Zanis, The microstructure and strength properties of MA957 nanostructured ferritic alloy joints produced by friction stir and electro-spark deposition welding, J. Nucl. Mater. 367–370 (2007) 1197–1202.
[14] C.L. Chen, G.J. Tatlock, A.R. Jones, Microstructural evolution in friction stir welding of nanostructured ODS alloys, J. Alloys Compd. 504 (2010) 460–466.
[15] H.H. Cho, H.N. Han, S.T. Hong, J.H. Park, Y.J. Kwon, S.H. Kim, R.J. Steel, Microstructural analysis of friction stir welded ferritic stainless steel, Mater. Sci. Eng. A 528 (2011) 2889–2894.
[16] B.W. Ahn, D.H. Choi, D.J. Kim, S.B. Jung, Microstructures and properties of friction stir welded 409L stainless steel using a Si3N4 tool, Mater. Sci. Eng. A 532 (2012) 476–479.
[17] R.S. Mishra, Z.Y. Ma, Friction stir welding and processing, Mater. Sci. Eng. R 50 (2005) 1–78.
[18] Z.L. Hu, X.S. Wang, Q. Pang, F. Huang, X.P. Qin, L. Hua, The effect of post processing on tensile property and microstructure evolution of friction stir welding aluminum alloy joint, Mater. Charact. 99 (2015) 180–187.
[19] R. Rai, A. De, H.K.D.H. Bhadeshia, T. DebRoy, Review: friction stir welding tools, Sci. Technol. Weld. Join. 16 (4) (2011) 325–342.
[20] R. Nafar Dehsorkhi, S. Sabooni, F. Karimzadeh, A. Rezaeian, M.H. Enayati, The effect of grain size and martensitic transformation on the wear behavior of AISI 304L stainless steel, Mater. Des. 64 (2014) 56–62.
[21] J.C. Lippold, D.J. Kotecki, Welding metallurgy and weldability of stainles steels, Wiley-Interscience, 2005.
[22] V. Shankar, T.P. Mannan, S. Sundaresan, Solidification cracking in austenitic stainless steel welds, Sadhana 28 (3–4) (2003) 359–382.
[23] Y.C. Chen, H. Fujii, T. Tsumura, Y. Kitagawa, K. Nakata, K. Ikeuchi, K. Matsubayashi, Y. Michishita, Y. Fujiya, J. Katoh, Banded structure and its distribution in friction stir processing of 316L austenitic stainless steel, J. Nucl. Mater. 420 (2012) 497–500.
[24] S.H.C. Park, Y.S. Sato, H. Kokawa, K. Okamoto, S. Hirano, M. Inagaki, Corrosion resistance of friction stir welded 304 stainless steel, Scr. Mater. 50 (2004) 101–105.
[25] S.H.C. Park, Y.S. Sato, H. Kokawa, K. Okamoto, S. Hirano, M. Inagaki, Rapid formation of the sigma phase in 304 stainless steel during friction stir welding, Scr. Mater. 49 (12) (2003) 1175–1180.
[26] C. Meran, M.B. Bilgin, Fusion and friction stir welding of X6Cr17 stainless steel, J. Achiev. Mater. Manuf. Eng. 61 (2) (2013) 403–410.
[27] H. Kokawa, S.H.C. Park, Y.S. Sato, K. Okamoto, S. Hirano, M. Inagaki, Microstructures in friction stir welded 304 austenitic stainless steel, Weld. World 49 (3–4) (2005) 34–40.
[28] W.C. Oliver, G.M. Pharr, An improved technique for determining hardness and elastic modulus using load and displacement sensing indentation experiments, J. Mater. Res. 7 (1992) 1564–1583.
[29] C.-C. Hsieh, W. Wu, Overview of intermetallic sigma (σ) phase precipitation in stainless steels, ISRN Metall. (2012) 1–16 (Article ID 732471).
[30] M. Schwind, J. Kallqvist, J.O. Nillson, J. Agren, H.O. Andren, σ phase precipitation in stabilized austenitic stainless steel, Acta Mater. 48 (2000) 2473–2781.
[31] R.A. Farrar, Microstructure and phase transformations in duplex 316 submerged arc weld metal, an ageing study at 700 °C, J. Mater. Sci. 20 (1985) 4215–4231.
[32] K. Ameyama, M. Hiromitsu, N. Imai, Room temperature recrystallization and ultrafine grain refinement of an SUS 316L stainless steel by high strain powder metallurgy process, Tetsu-to-Hagane 84 (5) (1998) 37–42.
[33] J.M. Vitek, S.A. David, Sigma phase transformation in austenitic stainless steel, Weld. J. 63 (8) (1984) 246.
[34] T. Saeid, A. Abdollah-zadeh, H. Assadi, F.M. Ghaini, Effect of friction stir welding speed on the microstructure and mechanical properties of a duplex stainless steel, Mater. Sci. Eng. A 496 (2008) 262–268.
[35] M. Esmailzadeh, M. Shamanian, A. Kermanpur, T. Saeid, Microstructure and mechanical properties of friction stir welded lean duplex stainless steel, Mater. Sci. Eng. A 561 (2013) 486–491.
[36] O. Frigaard, O. Grong, O.T. Midling, A process model for friction stir welding of age hardening aluminum alloy, Metall. Mater. Trans. A 32 (2001) 1189–1200.
[37] S.H.C. Park, Y.S. Sato, H. Kokawa, K. Okamoto, S. Hirano, M. Inagaki, Microstructural characterisation of stir zone containing residual ferrite in friction stir welded 304 austenitic stainless steel, Sci. Technol. Weld. Join. 10 (5) (2005) 550–556.

[38] S.F. Medina, C.A. Hernandez, General expression of the Zener–Hollomon parameter as a function of the chemical composition of low alloy and microalloyed steels, Acta Mater. 44 (1) (1996) 137–148.
[39] A.P. Reynolds, Flow visualization and simulation in FSW, Scr. Mater. 58 (2008) 338–342.
[40] A. Dehghan-Manshadi, P.D. Hodgson, Dependency of recrystallization mechanism to the initial grain size, Metall. Mater. Trans. A 39 (2008) 3830.
[41] M.H. Parsa, D. Ohadi, A constitutive equation for hot deformation range of 304 stainless steel considering grain sizes, Mater. Des. 52 (2013) 412–421.
[42] S. Sabooni, F. Karimzadeh, M.H. Enayati, Thermal stability study of ultrafine grained 304L stainless steel produced by martensitic process, J. Mater. Eng. Perform. 23 (5) (2014) 1665–1672.
[43] R. Ueji, H. Fujii, L. Cui, A. Nishioka, K. Kunishige, K. Nogi, Friction stir welding of ultrafine grained plain low-carbon steel formed by the martensite process, Mater. Sci. Eng. A 423 (2006) 324–330.
[44] Y. Sun, H. Fujii, Y. Takada, N. Tsuji, K. Nakata, K. Nogi, Microstructure and hardness distribution of friction stir welded 1050Al and IF steel with different original grain sizes, Trans. JWRI 38 (2) (2009) 43–48.